nature electronics

Supplementary information https://doi.org/10.1038/s41928-026-01581-9

A thermal-noise-resilient microwave quantum network up to 4 K

In the format provided by the authors and unedited

Supplementary Information for "A thermal-noise-resilient microwave quantum network up to 4 K"

CONTENTS

I. EXPERIMENTAL SETUP

A custom-designed microwave electronics chassis[1] is employed for qubit control and readout. An overview of the electronics configuration and cryogenic wiring is shown in Supplementary Fig. 1.

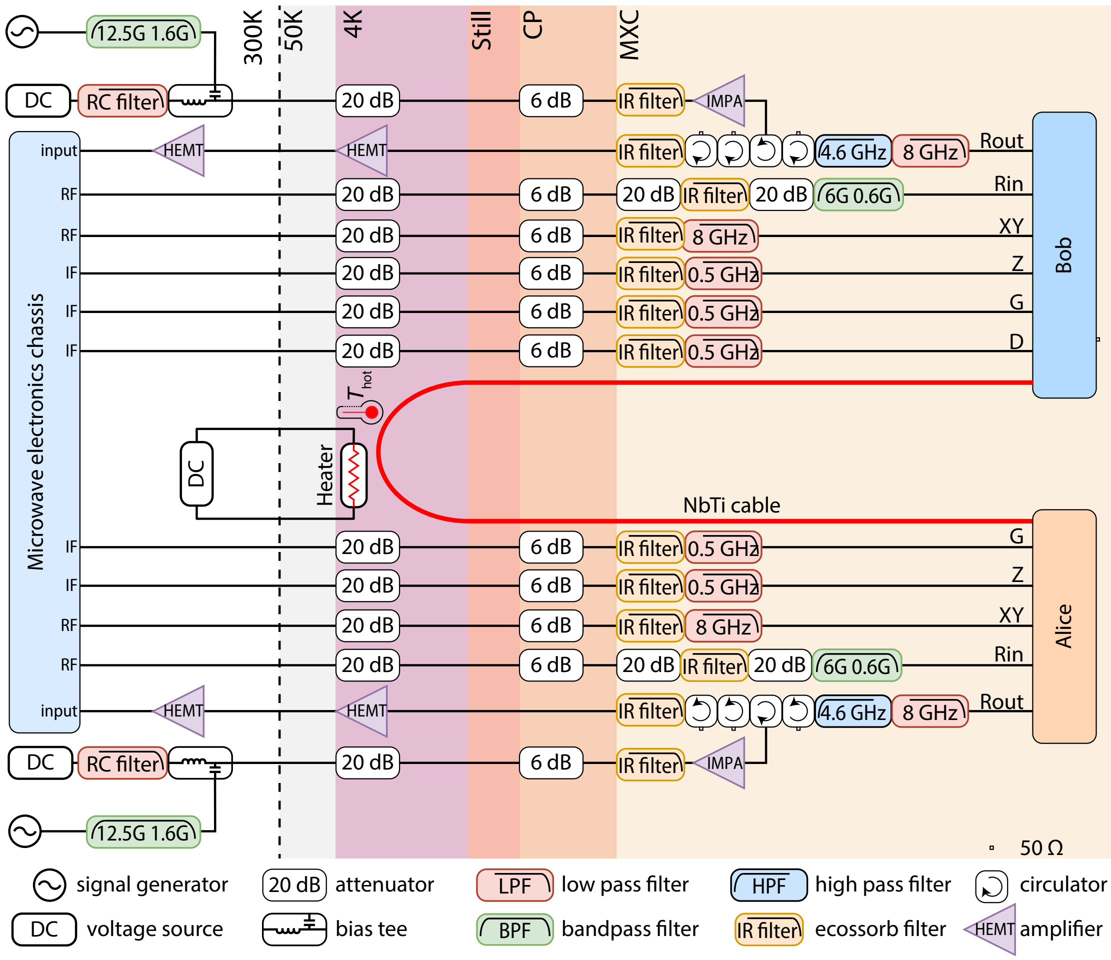

Supplementary Fig. 1. **Schematic of room-temperature electronics and cryogenic wiring.** The color-shaded regions represent different temperature stages of the dilution refrigerator. Labels indicate the corresponding refrigerator plates, where CP denotes the cold plate and MXC denotes the mixing chamber plate.

II. DEVICE INFORMATION

The design, measured parameters, and typical performance of each device component are summarized in Supplementary Table I. More details are provided in the subsections below.

The superconducting quantum chips for Alice and Bob share almost identical design, except that Alice does not have a D coupler. Both chips are fabricated from the same batch of sapphire wafer, on which a 100 nm-thick niobium thin film is deposited via magnetron sputtering at room

	setup 1		setup 2	
D coupler parameters	D		D	
coupler series capacitance, C_D (fF)	38.5		44.0	
coupler parasitic capacitance, C_p (fF)	17		23.5	
coupler SQUID inductance, $L_{D,0}$ (nH)	3.8		2.4	
coupler parasitic resistance, R_1 (Ω)	2300		2600	
minimum dissipation rate, $\kappa_D^{\min}$ (ms^{-1})	1/1.7		1/17.9	
maximum dissipation rate, $\kappa_D^{\max}$ (ns^{-1})	1/9.6		1/7.0	
qubit parameters	Q_A	Q_B	Q_A	Q_B
min freq., $\omega_q^{\min}/2\pi$ (GHz)	4.604	4.634	5.689	5.752
max freq., $\omega_q^{\max}/2\pi$ (GHz)	7.502	7.723	8.032	7.819
idling freq., $\omega_q/2\pi$ (GHz)	7.429	7.538	7.612	7.620
anharmonicity, $\eta/2\pi$ (MHz)	−204	−204	−200	−200
readout resonator freq., $\omega_{rr}/2\pi$ (GHz)	5.963	5.967	6.104	6.117
readout time (ns)	190	190	200	200
gmon coupler parameters	G_A	G_B	G_A	G_B
gmon junction inductance (nH)	0.6	0.6	1.5	1.5
gmon grounding inductance (nH)	0.2	0.2	0.3	0.3
channel parameters	NbTi cable	CPW	NbTi cable	CPW
inductance per unit length, $\mathcal{L}_j$ (nH/m)	240.5	402	240.5	402
capacitance per unit length, $\mathcal{C}_j$ (pF/m)	96.2	173	96.2	173
length (m)	1	0.0028	1	0.0027

Supplementary Table I. **Device parameters and typical performance.**

temperature. Most of the circuit elements are patterned on this niobium layer using lithography, followed by wet etching with an aqueous solution of hydrofluoric and nitric acids. The Josephson junctions are fabricated using the Dolan bridge method[2], with aluminum thin films deposited through electron-beam evaporation. After fabricating the Josephson junctions, an additional aluminum layer is deposited using lithography to form galvanic connections between the junctions and the base niobium film[3]. To suppress slotline modes, crossovers with SiO_2 scaffolds are used to connect the ground planes across the coplanar waveguides (CPWs) on the chip[4,5].

Following Ref.[6], quarter-wavelength ($\lambda/4$) CPW line impedance transformers are added between the gmon couplers and the bonding pads on both sides to reduce the interface loss. In the experimental setup 1 used in Figs.1-4 in the main text, we use identical $\lambda/4$ CPW lines for both Alice and Bob. It was later noticed that the interdigitated capacitor of the D coupler on Bob changes the resonant frequency of the $\lambda/4$ CPW line by a few hundred megahertz. This frequency mismatch for Alice and Bob makes it impossible to minimize interface loss on both sides simultaneously. In the experimental setup 2 used in Fig. 5 in the main text, we compensate this by adding a similar interdigitated capacitor to the Alice chip, together with a few other small modifications. This results in improvement in the cable mode lifetime from 820 ns to 1.4 μs, see Supplementary Section II C for details.

A. D coupler

Fast and tunable channel dissipation is crucial for our experiments involving thermal microwave photons. In our setup, this capability is realized using the D coupler, here the name "D" refers to dissipation. In this subsection, we provide a comprehensive description of the D coupler's design and performance.

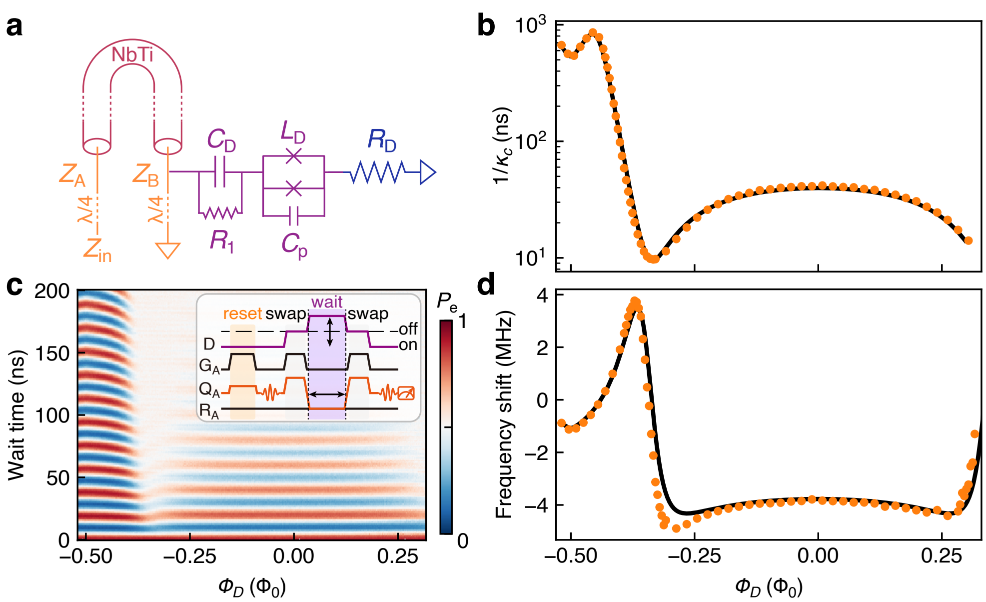

Supplementary Fig. 2. **Characterization of the D coupler.** **a**, Circuit model of the D coupler. The NbTi cable is connected to the D coupler circuit and shorted to ground. The D coupler consists of an interdigital capacitor C_D, a SQUID with an effective inductance L_D, and a parasitic capacitance C_p. The circuit is terminated by a 50 Ω load R_D, anchored to 10 mK, which provides dissipation. R_1 is parasitic resistance to account for the finite on/off ratio of the D coupler. **b**, Mode dissipation rate κ_c versus D coupler flux Φ_D. Φ_0 is a flux quantum. The orange dots represent the characteristic time of exponential fits to Fig. 2**b** of the main text. The solid line is given by calculation from the circuit model. **c**, Ramsey experiment traces of the mode R_s at various flux bias for the D coupler. Inset shows the control pulse sequence. **d**, Frequency shifts of R_c by Φ_D. The orange dots are the oscillation frequencies in **a** obtained by fitting. The solid line is given by calculation from the circuit model. The frequency shift is the shift compared to the D coupler off point.

As described in the main text, the D coupler comprises a DC SQUID in series with an interdigitated capacitor C_D. This circuit functions as a tunable bandpass filter, connecting the communication channel to a $R_D = 50\ \Omega$ cold load. The SQUID serves as a tunable inductance L_D, which can determine the passband frequency $\omega_D \approx 1/\sqrt{L_D C_D}$. At zero flux bias, $L_D = 3.8$ nH and the maximum $\omega_D/2\pi \approx 13$ GHz, encompassing the operating frequencies of the qubits. Note that the junction area also introduces a parasitic capacitance $C_p \approx 17$ fF. When the SQUID forms plasma resonance with C_p, the D coupler exhibits high impedance, effectively decoupling the channel from the cold load. Additionally, we account for a parasitic resistance R_1 due to the finite on/off ratio of the D coupler, as well as the $\lambda/4$ transformer that defines the cable boundary. The full circuit model is illustrated in Supplementary Fig. 2**a**.

We calculate the standing mode frequency and its quality factor using the circuit model by analyzing the input impedance from either side[7,8]. For example, on the Alice side, the input impedance is determined by the CPW terminated with the load Z_A, which is defined by the NbTi cable and the circuitry on the Bob side:

$$Z_{\rm in} = Z_t \frac{Z_A + iZ_t \tan(\beta_t l_t)}{Z_t + iZ_A \tan(\beta_t l_t)}, \tag{S1}$$

$$Z_A = Z_{\rm cb} \frac{Z_B + iZ_{\rm cb} \tan(\beta_{\rm cb} l_{\rm cb})}{Z_{\rm cb} + iZ_B \tan(\beta_{\rm cb} l_{\rm cb})}, \tag{S2}$$

$$Z_B = \left(\frac{1}{Z_D} + \frac{1}{iZ_t \tan \beta_t l_t}\right)^{-1}, \tag{S3}$$

$$Z_D = \left(i\omega C_D + \frac{1}{R_1}\right)^{-1} + \left(\frac{1}{i\omega L_D} + i\omega C_p\right)^{-1} + R_D, \tag{S4}$$

here $Z_j,\ \beta_j,\ l_j$ ($j = t, {\rm cb}$) are the characteristic impedance, wave vector and length of the $\lambda/4$ CPW line and the NbTi cable, respectively. The values of Z_j, β_j are determined by the inductance per unit length $\mathcal{L}_j$, and capacitance per unit length $\mathcal{C}_j$ through

$$Z_j = \sqrt{\mathcal{L}_j/\mathcal{C}_j}, \tag{S5}$$

$$\beta_j = \omega\sqrt{\mathcal{L}_j \mathcal{C}_j}. \tag{S6}$$

The specific values of $\mathcal{L}_j$ and $\mathcal{C}_j$ for the NbTi cable and the CPW line are summarized in Supplementary Table I.

By calculating $Z_{\rm in}(\omega)$ as a function of the angular frequency ω, we identify a series of zeros in ${\rm Im}[Z_{\rm in}(\omega)]$, corresponding to the resonance frequencies ω_m of the standing modes inductively coupled to the input port. The quality factor Q is given by[7]

$$Q = \omega_m/\kappa_D = \omega_m \frac{1}{{\rm Re}[Z_{\rm in}(\omega_m)]} \frac{1}{2} \frac{\partial {\rm Im}[Z_{\rm in}(\omega)]}{\partial \omega}\Big|_{\omega=\omega_m}. \tag{S7}$$

By tuning the bias flux Φ_D of the D coupler, the inductance $L_D = L_{D,0}/\cos(\pi\Phi_D/\Phi)$ is modified, resulting in changes to both the dissipation rate κ_D and the mode frequency ω_m. we consider the standing mode R_c at 7.48 GHz here and take intrinsic dissipation κ_i into account. The total dissipation rate of the mode is given by $\kappa_c = \kappa_i + \kappa_D$ where $\kappa_i = 1/820\ \text{ns}^{-1}$. The tunability of κ_c is demonstrated by measuring the energy relaxation of R_c in Fig. 2**b** of the main text, from which we extract the photon lifetime $1/\kappa_c$ through exponential fitting. The results shown as orange dots in Supplementary Fig. 2**b**.

The frequency shifts are experimentally measured through Ramsey experiments conducted at various Φ_D bias, as shown in Supplementary Fig. 2**c**. A superposition state $|0\rangle + |1\rangle$ is initialized on Q_A and then swapped into R_c. After tunning Φ_D to a specific value and waiting for a varying period t, we swap the photon back to Q_A, apply a second $\pi/2$ pulse, and then read out the qubit state. The observed oscillation of the excited-state probability P_e with t reflects the mode frequency $\omega_c/2\pi$ with high accuracy. By fitting the data to a sinusoidal function with an exponential decaying amplitude, the frequency shifts are extracted and shown as orange dots in Supplementary Fig. 2**d**. We notice that a distortion in the D bias pulse introduces slight asymmetry along $\Phi_D = 0$ in the measured frequency shifts.

To compare the experimental data with the predictions of the circuit model, we fit the model using the parameters $L_{D,0} = 3.8$ nH, $C_D = 38.5$ fF, $C_p = 17$ fF and $R_1 = 2300\ \Omega$. The calculated results, depicted as solid lines in Supplementary Figs. 2**b** and **d**, demonstrate the consistency between the model and the measurements. According to this model, we estimate that the minimum dissipation rate introduced by the D coupler at the "off" point is $\kappa_D^{\text{min}} = 1.7\ \text{ms}^{-1}$, far more smaller than the intrinsic dissipation rate of the mode and can be safely ignored.

B. Qubit readout and reset

When T_{hot} reaches 4.0 K, thermal noises diffuse to the quantum circuits through various degrees of freedom, and the coherence time of the qubits decrease to below 1 μs (see Supplementary Fig. 11**a** for details), necessitating fast qubit readout within a few hundred nanoseconds. To achieve this, we employ a Purcell filter[9–11] to facilitate rapid photon radiation from the readout resonator without compromising the qubit's relaxation time imposed by the Purcell effect[12–14]. The filter is centered at approximately 6 GHz, with a bandwidth of more than 100 MHz. Additionally, we employ a quantum-limited impedance-matched parametric amplifier (IMPA)[15,16] (as illustrated in the circuit diagram of Supplementary Fig. 1) to amplify the readout signal. The transmission spectrum of the readout feedline for Alice is shown in Supplementary Fig. 3**a**. With appropriate bias and pump power applied to the IMPA, the readout signal is amplified by approximately 25 dB over a bandwidth of 100 MHz, as shown in Supplementary Fig. 3**b**. Similar performance is also achieved for the IMPA of Bob.

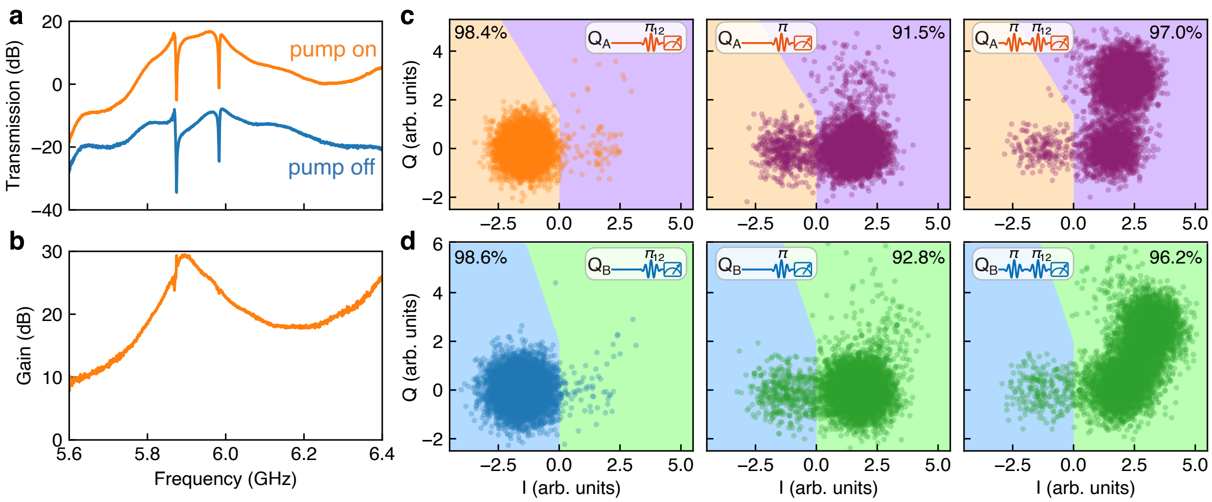

Supplementary Fig. 3. **Qubit readout performance.** **a**, Transmission spectrum of the readout feedline with/without IMPA pump. The bandpass feature comes from the integrated Purcell filter, whose passband matches the readout resonators. **b**, Gain profile of the IMPA extracted from **a**, demonstrating a gain of over 25 dB around the readout resonator frequency. **c, d**, Single-shot readout results of Q_A (c) and Q_B (d) at $T_{\rm hot} = 0.83$ K, with a readout pulse of 190 ns. The left column are IQ scatter data when the qubits are prepared in $|0\rangle$ state; The central column are IQ scatter data when the qubits are prepared in $|1\rangle$ state; The right column are IQ scatter data when the qubits are applied with a π_{12} pulse to transfer the population from $|1\rangle$ to $|2\rangle$ state. In the scatter plots, the orange (blue) shaded regions mark the assignment zone for the ground state of Q_A (Q_B), while the purple (green) regions denote the excited-state zones. Insets are the control sequences.

By combining the Purcell filter with the IMPA, we achieve rapid single-shot dispersive readout for both Q_A and Q_B within 190 ns, maintaining a separation error below 1%. However, the state preparation and measurement (SPAM) error remains significant, partly due to energy decay during the readout process. To further enhance the readout fidelity, we leverage the second excited state $|2\rangle$ to assist the qubit readout[17–19]. Before applying the readout pulse, a π_{12} pulse is applied to transfer the population from the $|1\rangle$ state to the $|2\rangle$ state. As the $|2\rangle$ state decays to $|1\rangle$ state first, then to the $|0\rangle$ state, this results in a longer process for the qubit to decay to the $|0\rangle$ state, thus enhancing the readout fidelity. Supplementary Figs. 3**c** and **d** show the single-shot readout results for Q_A and Q_B after prepared in the $|0\rangle$, $|1\rangle$ and $|2\rangle$ states, respectively. Leveraging the $|2\rangle$

state and discriminating between the $|0\rangle$ state and all the excited states (including $|1\rangle$ and $|2\rangle$), we achieve a reduced SPAM error below 4%. The qubit readout performance at elevated temperatures are shown in Supplementary Fig. 4 and Supplementary Fig. 9.

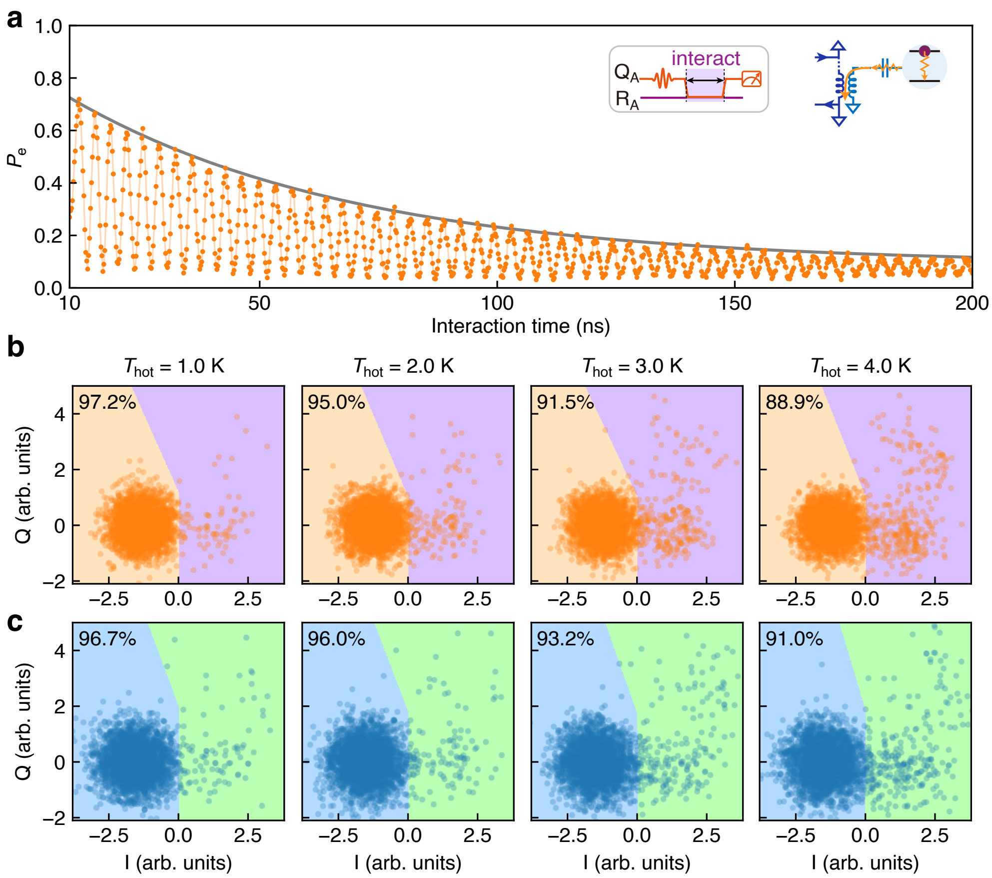

Supplementary Fig. 4. **Qubit reset with readout resonator.** **a**, Interaction between Q_A and the readout resonator R_A. The dots represent experimental data and the solid line shows the fit with a simple exponential function. Inset shows the control pulse sequence and the energy flow in this experiment. **b, c**, Single-shot readout results of Q_A (Q_B) after reaching equilibrium with readout resonator R_A (R_B). In the scatter plots, the orange (blue) shaded regions mark the assignment zone for the ground state of Q_A (Q_B), while the purple (green) regions denote the excited-state zones. Columns show data at different T_{hot}. Annotations indicate the proportion of results discriminating qubit at $|0\rangle$.

As demonstrated in Fig. 3 in the main text, the D coupler can effectively cool/reset both the cable modes and the qubits. However, there are scenarios where it is necessary to reset the qubits independently without perturbing the cable modes. For instance, during measurements of the cable mode lifetime in Fig.2**b** in the main text, it is essential to allow the cable modes to evolve freely while preventing the thermalization of the qubits. This is achieved by tuning the qubits into resonance with their readout resonators, which are well thermalized to 50 Ω loads anchored to the MXC stage through the feedline. The dissipation process through the readout resonator is illustrated in Supplementary Fig. 4**a**, where qubit Q_A is initially prepared in the $|1\rangle$ state and then tuned down into resonance with its readout resonator R_A. The energy rapidly swaps between Q_A and R_A with a period of approximately 3.2 ns, while the amplitude of oscillation decays over time with a characteristic time of about 60 ns, determined by the coupling quality factor of the readout resonator. Within 1 μs, the qubit reaches a steady state where its residual excitation is determined by its environmental temperature. The equilibrium populations of Q_A and Q_B after the dissipation process are shown in Supplementary Figs. 4**b** and **c**, respectively. For Q_A, the excitation populations are reduced to 2.8%, 5.0%, 8.5%, and 11.1% at $T_{\rm hot} = 1$ K, 2 K, 3 K and 4 K, respectively. Similarly, for Q_B, the populations are suppressed to 3.3%, 4.0%, 6.8%, and 9.0% under the same conditions. Although these excitation populations are slightly higher than those achieved using the D coupler for qubit reset (see Fig. 3 in the main text and Supplementary Fig. 9 for more details), they remain significantly lower than the equilibrium excitation populations without any reset (see Supplementary Fig. 9**b**). These results indicate that the readout resonators provide an effective alternative method for resetting the qubits.

C. Cable benchmark

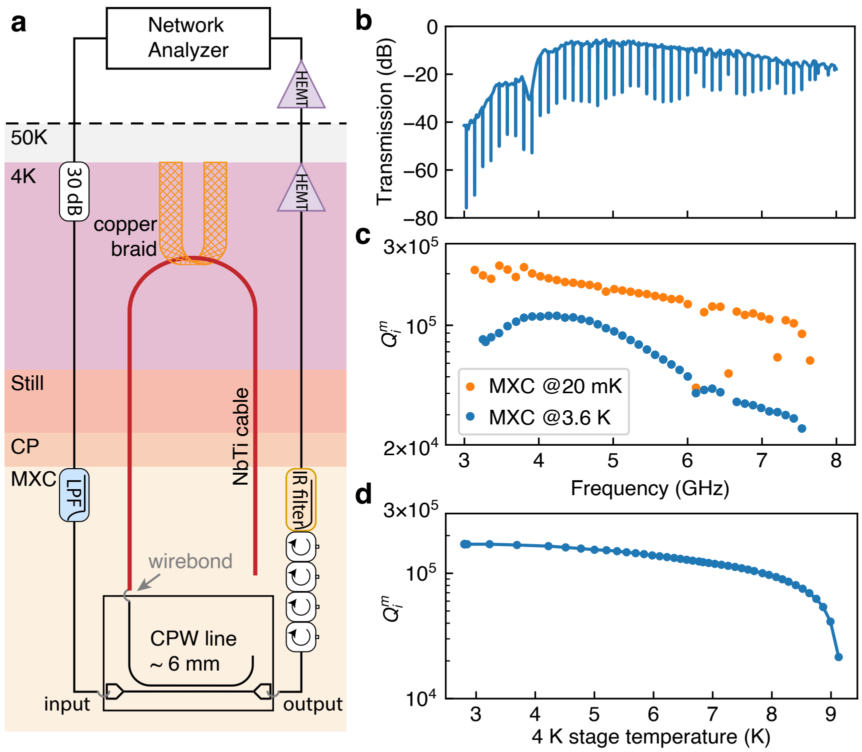

Supplementary Fig. 5. **Independent cable test.** **a**, Setup for measuring the quality factor of the cable modes. The center of the NbTi cable is thermally anchored to the 4 K stage using copper braid. The color-shaded regions represent different temperature stages of the dilution refrigerator. **b**, Transmission spectroscopy of the test chip, showing a series of evenly spaced sharp dips, corresponding to the standing wave modes hosted within the cable. **c**, Internal quality factors Q_i^m of the cable modes, obtained at the MXC stage temperature of 20 mK and 3.6 K respectively. **d**, Q_i^m of the 4.35 GHz mode versus the 4 K plate temperature as the DR warms up.

The NbTi cable used in this experiment, purchased from Keycom Corp., has a superconducting transition temperature of approximately 9.7 K. In this section, we perform an independent spectroscopy measurement to characterize the quality factor of the cable under various temperatures, as shown in Supplementary Fig. 5. For these tests, the center of the NbTi cable is thermally anchored to the 4 K stage of the DR using copper braid. One end of the cable is wire-bonded to a dedicated test chip, while the other end is left open. On the test chip, the cable is connected to a CPW line, which is patterned on a niobium thin film deposited on a sapphire substrate. The CPW line is approximately 6 mm in length and inductively coupled to a feedline in a hanger geometry before shorted to ground. The CPW line serves as a quarter-wavelength impedance transformer centered at around 4 GHz[6]. We measure the transmission spectrum of the feedline using a vector network analyzer (VNA).

Before condensing the ^{3}He-^{4}He mixture to the DR, the 4 K, still, and MXC stages are maintained at 3.6 K. We perform VNA measurement at this temperature and observe a series of evenly spaced sharp dips in the transmission spectrum (see Supplementary Fig. 5**b**), corresponding to the standing wave modes hosted within the cable. After condensing ^{3}He-^{4}He mixture to the DR, the 4 K stage maintains at 3.6 K, but the still stage quickly cools to 0.83 K, and the MXC stage gradually cools to about 20 mK. We measure the transmission spectrum and extract the internal quality factors[20,21] Q_i^m of the m-th cable mode under these two temperature conditions, as shown in Supplementary Fig. 5**c**. The cable modes show relatively high intrinsic quality of $\sim 2 \times 10^5$ near 4 GHz, where the 6 mm CPW line minimizes the wirebond loss. To investigate the cable performance at even higher temperatures, we monitor the 4.35 GHz mode as the DR warms up. The variation in the quality factor as the 4 K stage temperature increases is shown in Supplementary Fig. 5**d**. Remarkably, the quality factor exhibits no significant degradation until the 4 K stage temperature approaches 8.5 K, close to the 9.7 K superconducting transition temperature of NbTi. This observation indicates that the intrinsic loss rate κ_i of the cable mode to the thermal environment remains low within the temperature range of interest. Such robustness is critical for the dynamical reduction of thermal noise in our experiment. We note that the observed Q_i^m of $\sim 2 \times 10^5$ is similar to the NbTi cable quality factors reported in Refs. 11,22,23.

Because the thermal occupation decreases with the operating frequency, we choose to operate at higher frequencies, and shorten the $\lambda/4$ CPW line to 2.8 mm to align the standing mode to approximately 7 GHz in Alice and Bob. In Supplementary Fig. 6, we present the quality factors derived from the single-photon lifetime measurements similar to that in Fig.2**b** of the main text, with the D coupler turned off. We see that the mode at around 7 GHz exhibits the highest quality of about 4.4×10^4. The mode R_c at 7.48 GHz has a slightly lower quality factor, but its frequency is closer to the maximum qubit frequency, therefore we choose this mode for communication in the end. The quality of the standing modes in the quantum communication setup is much smaller than the results from the cable test in Supplementary Fig. 5, partly because the NbTi cable quality degrades at higher frequencies[22,23]. Also it is more difficult to match both cable-chip joints simultaneously to a single mode, especially at higher operating frequencies.

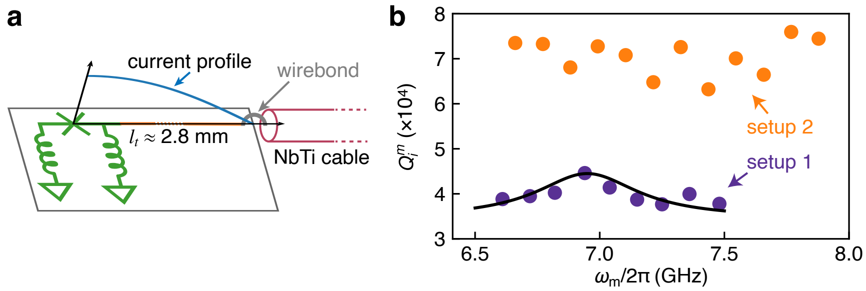

Supplementary Fig. 6. **Quality factors of the standing modes in the communication channel. a**, Schematic showing the standing mode current profile along the $\lambda/4$ impedance transformer. When frequency matched, the current node coincides with the wirebond joint. **b**, The Q_i^m of each mode versus the mode frequency $\omega_m/2\pi$, calculated from the single-photon lifetime. The solid line is fitted using the equation from Ref. 6. The cable mode quality factors of the setup 2 are almost doubled compared to the setup 1, although there is no obvious peak in the trend, likely because the quality factors become limited by other factors.

Since the CPW line impedance transformer is connected to both the wirebond interface and the dissipator D, it plays a crucial role in determining the cable mode coherence. In the setup 1, we simply use identical CPW line designs for Alice and Bob. It is later noticed that the large capacitance C_p of the dissipator D alters the boundary condition of the CPW transformer on Bob, leading to a frequency shift of several hundred megahertz. This shift causes a mismatch between the transformer on Bob's chip, where the dissipator is present, and that on Alice's chip, where it is absent. To compensate for this effect, a similar capacitor as that in the D coupler is added to the Alice chip in the setup 2. In addition, several small modifications are also made to reduce the channel loss. First, the length of the transformer is shortened from 2.8 mm to 2.7 mm to better match the operating frequency. Second, the crossovers with lossy SiO_2 scaffold across the transformer are removed to reduce dielectric loss. Finally we achieve a noticeable improvement of the cable mode lifetime, with T_{1r} increasing from 820 ns at 7.48 GHz to 1.4 μs at 7.66 GHz, nearly doubling the internal quality factor Q_i, see Supplementary Fig. 6**b**.

III. QUANTUM THERMODYNAMICS

The thermal microwave channel with tunable dissipation in this experiment allows us to explore quantum thermodynamics in engineered cryogenic environments[24–29]. In particular, fast switching of the channel dissipation enables time-domain control of energy exchange and thermalization, allowing us to directly probe non-equilibrium dynamics as a function of the channel temperature.

A. Qubit-channel interaction at various temperatures

As the decoherence rates remain lower than the interaction rate ($g_n^m/2\pi \approx 5$ MHz) between the qubits and the cable modes, coherent interactions between them are readily observable. In Supplementary Fig. 7**a**, we demonstrate vacuum Rabi oscillations between Q_A and the cable modes. An illustration of the control sequence and experimental diagram is shown on the left. The D coupler is initially turned on to reset both the qubit and cable modes (see Supplementary Fig. 8 for details). A subsequent π-pulse prepares Q_A in its first excited state $|1\rangle$. We then vary the qubit frequency to interact with each mode. During the interaction, the D coupler is turned "off" to avoid loss of coherent photons. By measuring the excitation probability P_e of Q_A, we observe coherent vacuum Rabi oscillations between the qubit and the modes across a T_{hot} range from 1 K to 4 K. Although faster rethermalization of the modes at $T_{\text{hot}} = 4$ K leads to more rapid decay of the coherent oscillations, coherent exchange remains observable up to a few hundred nanoseconds, ensuring reliable quantum state transfer through the channel.

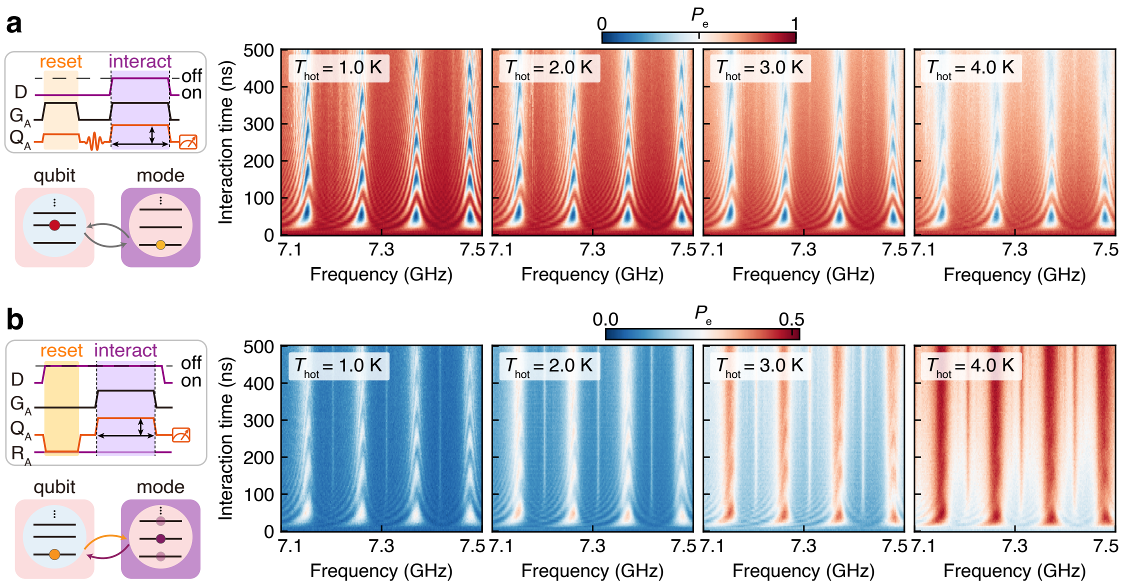

Supplementary Fig. 7. **Interaction between Q_A and cable modes at different T_{hot}.** **a**, Vacuum Rabi oscillations between Q_A and the radiatively cooled cable modes at various T_{hot}. The thermal photons in each mode are dynamically reduced by radiative cooling prior to the interaction. **b**, Interaction between Q_A and the warm cable modes without prior cooling. We first reset Q_A by tuning into resonance with its readout resonator R_A, then use it to detect the thermal photons in the cable modes. Left: the experimental control sequence and schematic diagram.

Coherent oscillations are also evident between the qubit and thermal photons within the modes. In Supplementary Fig. 7**b**, we demonstrate the interaction between Q_A, initialized in the $|0\rangle$ state, and the cable modes with high thermal occupation. To achieve this, we set the D coupler to the "off" point, where the standing modes remain warm, while resetting Q_A alone by tuning it into resonance with its readout resonator R_A (see Supplementary Fig. 4). Subsequently, we tune up the G_A coupler to a coupling strength of $g_A^m/2\pi \approx 5$ MHz, and vary the frequency of Q_A to interact with different standing-wave modes. The thermal photons initially present in the modes are exchanged between the qubit and the modes, resulting in a clearly visible oscillation chevron pattern at $T_{\text{hot}} = 1.0$ K, indicative of a primary thermal population in the $|1\rangle$ Fock state. As T_{hot} increases, the chevron patterns gradually fade out, reflecting the rapid degradation of the system coherence with increased thermal noise.

B. Cooling and rethermalization at various temperatures

In the main text, we discussed the cooling and rethermalization dynamics of the qubit-mode system at $T_{\text{hot}} = 4.0$ K. Here, in Supplementary Fig. 8, we extend to various T_{hot} values, focusing on the mode R_c, to evaluate the performance of the D coupler in cooling both the qubit and the thermal channel. To cool/reset the qubit, we activate the gmon coupler and tune the qubit into resonance with the radiatively cooled mode R_c, keeping the D coupler in the "on" state throughout the process. The time evolution of the qubit excitation probability, P_e, is shown in Supplementary Figs. 8**a** and **b**, revealing the cooling dynamics. The qubits are effectively reset to their ground state, with residual thermal excitation of $P_e = 0.016$, 0.034, 0.041, and 0.095 for Q_A, and $P_e =$ 0.019, 0.035, 0.056, and 0.086 for Q_B, corresponding to $T_{\text{hot}} = 1$ K, 2 K, 3 K and 4 K, respectively.

As long as the D coupler is kept in the "on" state, both the qubit and the thermal channel can be effectively cooled through dissipation to the cold bath. However, to enable the coherent transmission of microwave quantum states through the channel, the D coupler must be temporarily turned "off" to prevent the loss of coherent photons. During this interval, both the thermal channel and the qubit undergo rethermalization, and the rethermalization rate becomes a critical parameter for achieving efficient quantum state transfer. To investigate the rethermalization dynamics, we monitor the thermal occupation of the channel after the D coupler is turned "off". As illustrated in Supplementary Figs. 8**c** and **d**, the D coupler is first turned "on" to reset both the qubit and the channel effectively. It is then temporarily switched "off" while the gmon coupler is activated, allowing the qubit to interact with R_c and reach thermal equilibrium. The rethermalization of the channel is quantified by tracking the time evolution of P_e. At equilibrium, the qubits exhibit steady-state excitation probabilities of $P_e = 0.26$, 0.35, 0.45 and 0.56 for Q_A, and $P_e = 0.26$, 0.35, 0.44, and 0.52 for Q_B, at $T_{\rm hot} = 1$ K, 2 K, 3 K and 4 K, respectively. In Supplementary Fig. 8, we use simple exponential fitting to characterize the cooling and rethermalization of the system, which shows a typical cooling time of 50 ns, and a typical rethermalization time of $1 \sim 2$ μs. These values serve as a guidance for the quantum state transfer experiments, which are completed within 1/10 of the characteristic rethermalization time. A more careful numerical simulation of the system dynamics based on master equations is given in Supplementary Section III C.

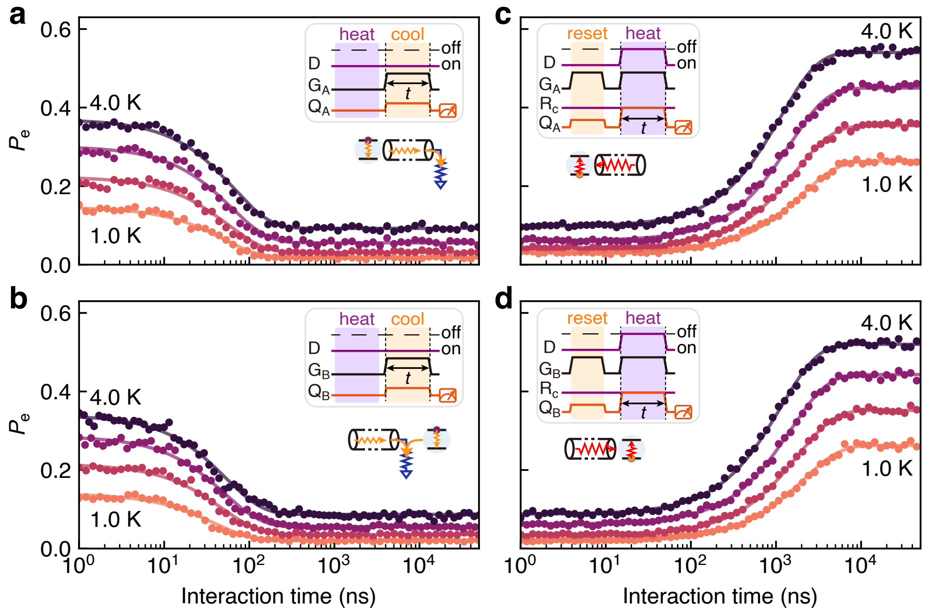

Supplementary Fig. 8. **Cooling and rethermalization at various $T_{\rm hot}$. a**, **b**, Cooling of Q_A amd Q_B through the mode R_c at different $T_{\rm hot}$, with the D coupler suddenly turned to the "on" state. The qubits are initially in a thermal state characterized in Supplementary Fig. 9**b**, where both the gmon coupler and the D coupler are off. The solid lines are simple exponential fits with characteristic time of 56 ns, 55 ns, 61 ns, and 65 ns for Q_A, and 40 ns, 49 ns, 50 ns, and 52 ns for Q_B, at $T_{\rm hot} = 1$ K, 2 K, 3 K, 4 K, respectively. **c**, **d**, Rethermalization of Q_A and Q_B when coupled to R_c at various $T_{\rm hot}$, where the D coupler is suddenly turned to the "off" state. Both the qubits and R_c are initially reset to their ground states. The qubits are tuned into resonance with R_c while the D coupler is turned off, resulting in thermalization of the qubits to a steady state with a higher excitation probability P_e (see Supplementary Fig. 9**c**). The solid lines represent exponential fits with characteristic time of $\tau = 1.97$ μs, 1.72 μs, 1.41 μs, and 1.14 μs for Q_A, and 2.06 μs, 1.76 μs, 1.49 μs, and 1.15 μs for Q_B, at $T_{\rm hot} = 1$ K, 2 K, 3 K, 4 K, respectively. Inset shows the control sequences and illustration on the thermal photon flow.

Supplementary Fig. 9 provides further details about the steady states of Q_A. The single-shot dispersive readout results of Q_A are presented in the quadrature (IQ) space, obtained after 6000 repetitions. In Supplementary Fig. 9**a** we present the readout results of steady state with both G_A and D couplers turned on, corresponding to the final state after the cooling process in Supplementary Fig. 8**a**. The ground state population P_0 is annotated in the upper left corner of each panel. Thermal excitations are largely suppressed for all $T_{\rm hot}$, resulting in $P_e < 0.1$ even at 4 K.

In Supplementary Fig. 9**b**, the steady state of Q_A is displayed with both G_A and D couplers turned off. This corresponds to the initial state of the cooling process in Supplementary Fig. 8**a**, where the qubit should be decoupled from the warm channel ideally. However, significant thermal excitations are observed, with P_e increasing from 0.13 at $T_{\rm hot} = 1$ K to 0.34 at $T_{\rm hot} = 4$ K. Signatures of $|2\rangle$ or higher-level occupancy also become evident. These results suggest that thermal noise from the warm channel cannot be fully isolated by the gmon coupler. Further improvements, such as implementing bandpass filters or quasiparticle suppression techniques, may enhance the system's thermal isolation and overall performance.

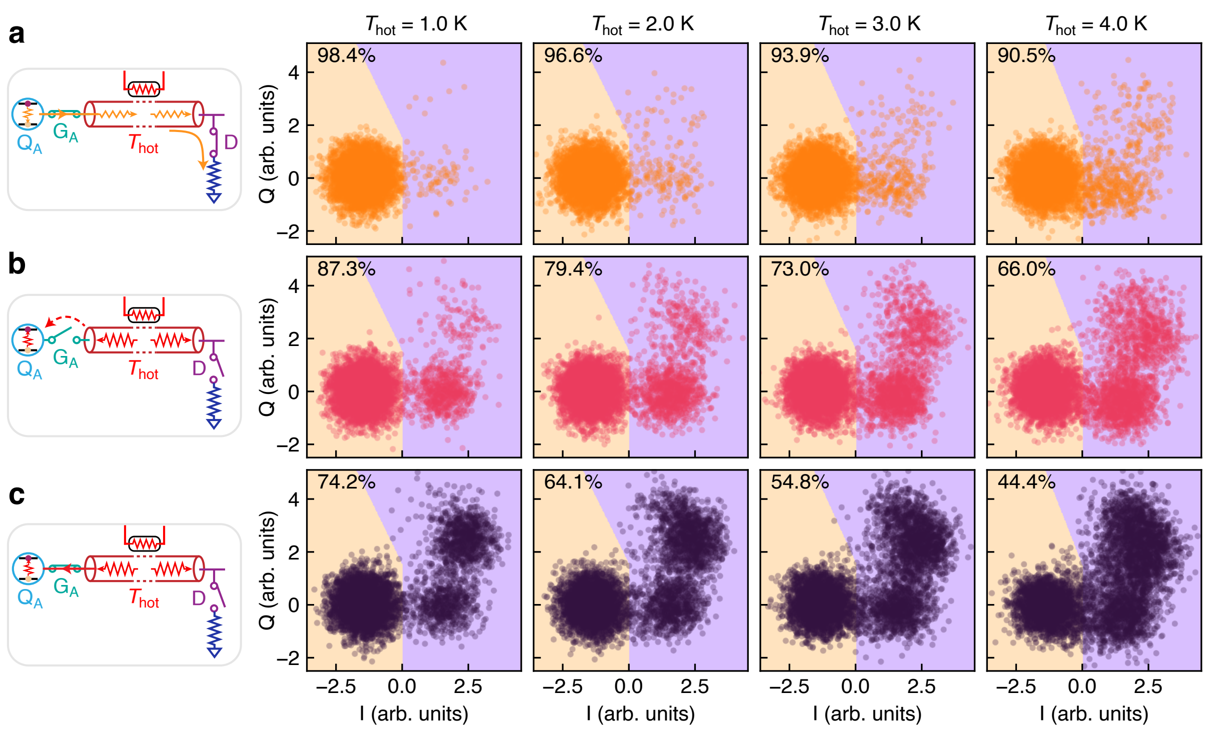

Supplementary Fig. 9. **Qubit steady states under different configurations.** Single-shot dispersive readout results in the quadrature (IQ) space of Q_A after reaching equilibrium with **a** both the G_A and D couplers are turned on; **b** both the G_A and D couplers are turned off; **c** G_A is turned on while D is turned off. The left illustrates the thermal noise flow in these cases. In the scatter plots, the yellow shaded regions mark the assignment zone for the ground state of Q_A, while the purple regions denote the excited-state zones. Columns show data at different $T_{\rm hot}$. Annotations indicate the proportion of results discriminating the qubit in the $|0\rangle$ state.

In Supplementary Fig. 9**c**, we demonstrate the impact of thermal noise when the D coupler is turned "off", while G_A remains switched on. This corresponds to the final state of the rethermalization process in Supplementary Fig. 8**c**. In this configuration, thermal excitation P_e exceeds 0.3 at $T_{\text{hot}} = 1.0$ K, and even surpasses 0.5 at $T_{\text{hot}} = 4.0$ K, making reliable qubit state preparation infeasible.

C. Numerical simulation

Modeling the system dynamics with multiple bosonic modes, which are occupied with a large number of thermal photons, is complicated. Since the qubit-mode coupling $g_n^m \ll \omega_{\text{FSR}}$ in the quantum communication experiment, we can ignore irrelevant modes and restrict Eq. (1) in the main text to a single bosonic mode R_c:

$$H/\hbar = \sum_{n=A,B} (\omega_n \sigma_n^\dagger \sigma_n + \frac{\eta}{2} \sigma_n^\dagger \sigma_n^\dagger \sigma_n \sigma_n) + \omega_c a_c^\dagger a_c + \sum_{n=A,B} g_n^c (\sigma_n^\dagger a_c + \sigma_n a_c^\dagger), \tag{S8}$$

where σ_n and a_c represent the annihilation operators for qubit Q_n and the cable mode R_c at 7.48 GHz, respectively. The qubits are modeled as Duffing oscillators with anharmonicity η. To account for system decoherence in the presence of a thermal environment, we analyze the dynamics of the system's density matrix ρ using the Lindblad master equation under the Born-Markov approximation:

$$\dot{\rho}(t) = \frac{1}{i\hbar}[H, \rho(t)] + \sum_j \frac{1}{2} \left[2L_j \rho(t) L_j^\dagger - \rho(t) L_j^\dagger L_j - L_j^\dagger L_j \rho(t) \right], \tag{S9}$$

with the corresponding Lindblad operators L_j[30]:

$$L_{\phi,n} = \sqrt{\Gamma_\phi/2} \left(\sigma_n^\dagger \sigma_n \right), \tag{S10}$$

$$L_{\downarrow,n} = \sqrt{\kappa_n(\langle N_n \rangle + 1)} \sigma_n, \tag{S11}$$

$$L_{\downarrow,c} = \sqrt{\kappa_c(\langle N_c \rangle + 1)} a_c, \tag{S12}$$

$$L_{\uparrow,n} = \sqrt{\kappa_n \langle N_n \rangle} \sigma_n^\dagger, \tag{S13}$$

$$L_{\uparrow,c} = \sqrt{\kappa_c \langle N_c \rangle} a_c^\dagger. \tag{S14}$$

The first term represents the pure dephasing of the qubits; the subsequent terms describe the relaxation of each component of the system toward a thermal state with an effective rate $\sim \kappa_j(\langle N_j \rangle + 1)$ ($j = A, B, c$). Here, κ_j denotes the coupling rate between the system and its thermal bath, and $\langle N_j \rangle$ is the average thermal occupation in the bath, as illustrated in Supplementary Fig. 10.

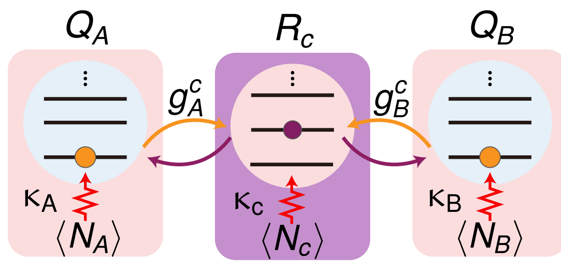

Supplementary Fig. 10. **Quantum thermodynamics model for the system.** Two qubits are coupled to the communication mode R_c. Each component is also coupled to an effective heat bath characterized by the coupling rate κ_j and thermal occupancy $\langle N_j \rangle$ ($j = A$, B, c).

The effective environment of the system is a composite of all thermal baths coupled to its components. For example, the communication mode R_c interacts with two baths: the thermal environment characterized by an average photon number $\langle N_e \rangle$ and coupling rate κ_i, and the 50 Ω cold load with an average photon number $\langle N_{\text{cold}} \rangle$ and coupling rate κ_D. The combined effect of these baths can be equivalently described by an effective environment with the following parameters:

$$\langle N_c \rangle = \frac{\kappa_i \langle N_e \rangle + \kappa_D \langle N_{\text{cold}} \rangle}{\kappa_i + \kappa_D}, \tag{S15}$$

$$\kappa_c = \kappa_i + \kappa_D, \tag{S16}$$

which simplifies the analysis of the system's thermal dynamics.

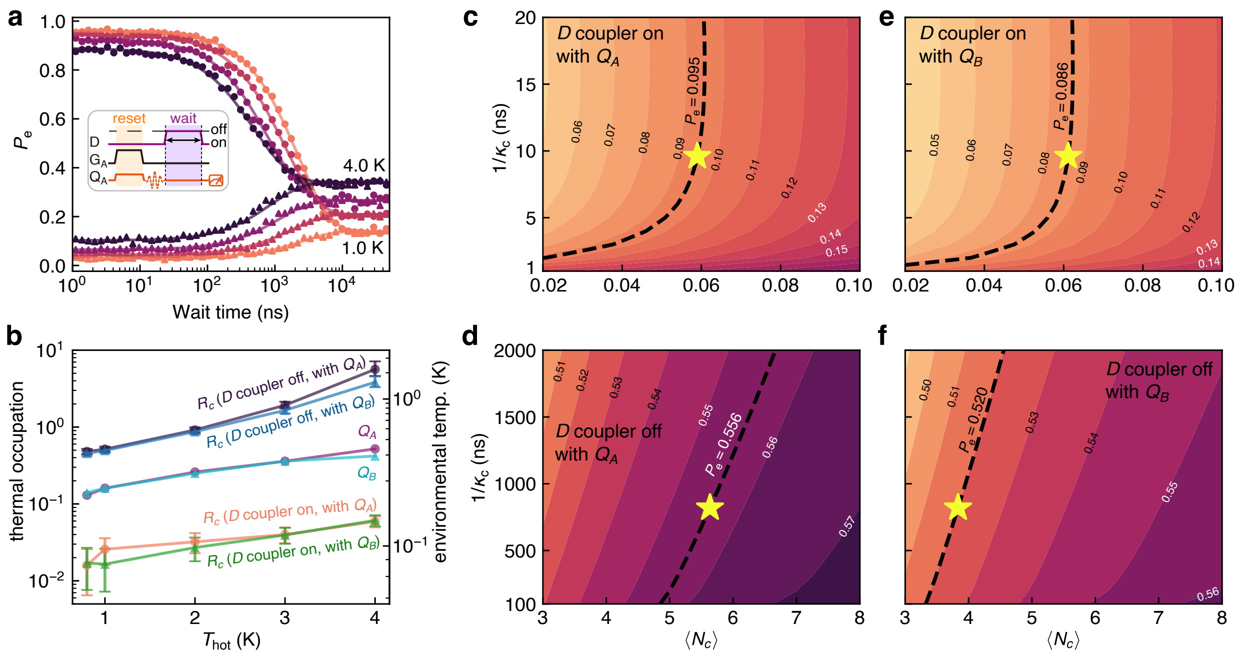

Supplementary Fig. 11. **Estimation of effective temperature and thermal photon occupancy.** **a**, Evolution of $|1\rangle$ state relaxation (circle dots) and $|0\rangle$ state thermalization (triangular dots) of Q_A at various T_{hot} from 1 K to 4 K. Solid lines are master equation simulation results. Inset shows the control sequence. **b**, The thermal photon occupancy, as well as the effective environmental temperature for both qubits, and R_c with D coupler on and off, respectively. Data for the qubits are from master equation simulations in **a**. Data for mode R_c are estimated from steady state analysis using either Q_A (circle dots) or Q_B (triangular dots) shown in (**d**–**f**). Errorbars for R_c are estimated assuming a ± 0.01 variation in the qubit steady state P_e. **c**, **d**, Numerical steady state P_e of Q_A when coupled to R_c, as a function of $\langle N_c \rangle$ and κ_c at $T_{\mathrm{hot}} = 4.0$ K. κ_A and $\langle N_A \rangle$ are taken from the fitting results in **a**. The dashed lines are contours for the experimentally observed value of $P_e = 0.095$ and 0.556 respectively. The stars indicate the points where κ_c matches the value measured at $T_{\mathrm{hot}} = 0.83$ K. **e**, **f**, Steady state P_e of Q_B coupled to R_c at $T_{\mathrm{hot}} = 4$ K, similar to **c** and **d**.

We numerically simulate the system dynamics described by Eq. S8 and Eq. S9 using QuTiP[31]. By fitting the simulation results to experimental data, we estimate system parameters, including the number of thermal photons in the environment $\langle N_j \rangle$ and the system-environment coupling rate κ_j. In Supplementary Fig. 11**a**, we compare the numerical simulations with $|1\rangle$ state relaxation and $|0\rangle$ state thermalization of Q_A at various T_{hot}. Importantly, the simulations do not assume a perfect initial state ($|0\rangle$ or $|1\rangle$) but instead start with a mixed state characterized by the initial P_e, which is set to the experimentally measured value at the beginning of the evolution. Focusing solely on Q_A (Q_B) while neglecting contributions from other components, the fitted parameters for Q_A (Q_B) are summarized in Supplementary Table II, and the thermal occupancy is plotted in Supplementary Fig. 11**b**. The observed decrease in $1/\kappa_A$ ($1/\kappa_B$) with T_{hot} suggests that the the qubit coherence degrades as the thermal noise level increases. The effective temperatures are calculated from the thermal occupancy according to the Bose-Einstein distribution.

T_{hot}	0.83 K	1.0 K	2.0 K	3.0 K	4.0 K
$1/\kappa_A$	2.74 μs	2.80 μs	2.05 μs	1.37 μs	1.08 μs
$\langle N_A \rangle$	0.13	0.16	0.26	0.36	0.52
$1/\kappa_B$	3.54 μs	3.48 μs	2.75 μs	1.83 μs	1.30 μs
$\langle N_B \rangle$	0.14	0.16	0.25	0.36	0.42
$\langle N_c \rangle$ (D coupler on, with Q_A)	0.016	0.026	0.032	0.040	0.059
$\langle N_c \rangle$ (D coupler on, with Q_B)	0.017	0.017	0.027	0.039	0.061
$\langle N_c \rangle$ (D coupler off, with Q_A)	0.48	0.52	0.92	1.92	5.64
$\langle N_c \rangle$ (D coupler off, with Q_B)	0.46	0.50	0.87	1.65	3.83

Supplementary Table II. **Thermodynamic parameters of the system.** κ_n and $\langle N_n \rangle$ ($n = A, B$) are fitted parameters obtained from the numerical simulations as shown in Supplementary Fig. 11**a**. The thermal occupancy $\langle N_c \rangle$ for R_c is estimated from the steady state analysis using Q_A or Q_B, as shown in in Supplementary Figs. 11**c** to **f**.

In addition to analyzing the qubits alone, it is crucial to estimate the thermal occupation of the cable mode R_c, with or without radiative cooling. As mentioned in the main text, superconducting qubits based microwave thermometry has been demonstrated at sub-Kelvin temperatures[32–34], but extending these methods to liquid helium temperature is quite challenging. We note that the simulation of the qubit dynamics in Supplementary Fig. 11**a** is valid because the thermal occupancy of the qubit alone is small (see Supplementary Table II). With many thermal photons in the channel, simulating the system dynamics becomes infeasible, as the state preparation and measurement processes are spoiled by thermal noise. Here we instead adopt a steady state approach, which is done by comparing the system's steady state in numerical simulation with the experimentally measured steady state P_e from Supplementary Fig. 9, see Supplementary Figs. 11**c** to **f**. The steady state analysis is robust against errors introduced by qubit decay and rethermalization during the measurement process. Furthermore, the steady state P_e is predominantly determined by the thermal occupancy $\langle N_j \rangle$ and the system-environment coupling rate κ_j ($j = A$, B, c), regardless of the system initial state. As shown in Supplementary Figs. 11**c** to **f**, we observe a clear dependence of the steady state P_e on κ_c and $\langle N_c \rangle$. Supplementary Figs. 11**c** and **d** highlight the steady state P_e

of Q_A, corresponding to the configuration where the D coupler is turned "on"and "off" respectively. The black dashed lines in Supplementary Figs. 11**c** and **d** are contours for $P_e = 0.095$ and 0.556, corresponding to the experimentally measured steady state excitation of Q_A at $T_{\text{hot}} = 4.0$ K with the D coupler is "on" (Supplementary Fig. 9**a**) and "off" (Supplementary Fig. 9**c**), respectively. The yellow stars in Supplementary Figs. 11**c** and **d** indicate the probable parameters based on the mode coherence measured at $T_{\text{hot}} = 0.83$ K (see Fig. 2 in the main text). The variation, along with the estimated values marked by the yellow stars, is plotted in Supplementary Fig. 11**b** for various T_{hot}. At $T_{\text{hot}} = 4.0$ K, we estimate $\langle N_c \rangle \approx 5.64$ when the D coupler is turned "off". Conversely, when the D coupler is turned "on", we estimate $\langle N_c \rangle \approx 0.06$. Similar steady state analysis of R_c, but instead using the steady state excitation of Q_B for estimation, is shown in Supplementary Figs. 11**e** and **f**. We again confirm $\langle N_c \rangle \approx 0.06$ when the D coupler is turned "on", but there is observable discrepancy for the thermal occupancy when the D coupler is turned "off", estimated using different qubits, suggesting this method is also limited when there is large thermal photons in the system. If we take an average of the results from both qubits, we have $\langle N_c \rangle \approx 4.73$. This corresponds to a thermal photon reduction ratio of 79, very close to the estimation of 86 in the main text using κ_i and κ_D measured at $T_{\text{hot}} = 0.83$ K.

IV. STATE TRANSFER AND REMOTE ENTANGLEMENT AT OTHER TEMPERATURES

In Fig. 4 of the main text, we show the quantum state transfer and remote entanglement generation through the thermal channel at $T_{\text{hot}} = 4$ K using the experimental setup 1. Supplementary Fig. 12 extends these results to a range of channel temperatures, $T_{\text{hot}} = 0.83$ K, 1 K, 2 K, and 3 K, respectively. In Supplementary Fig. 12**a**, we show the transfer of a single photon from Q_A to Q_B via mode R_c. This process follows the same pulse sequence described in Fig. 4 of the main text, where the D coupler is turned "off", and both G_A and G_B are activated with matching coupling strengths ($g_A^c = g_B^c \approx 2\pi \times 5$ MHz). After an evolution time of $t = 65$ ns, the photon population in Q_B reaches its maximum. The efficiency of quantum state transfer is characterized using quantum process tomography[11], with the reconstructed process matrices χ displayed in Supplementary Fig. 12**b**. The corresponding process fidelities, $\mathcal{F}_\chi$, are determined to be 90.0%, 88.3%, 79.3%, and 67.5% for $T_{\text{hot}} = 0.83$ K, 1 K, 2 K, and 3 K, respectively. These fidelities are calculated directly from the raw data, while the values highlighted by orange frames in Supplementary Fig. 12**b** represent the corrected fidelities after applying the SPAM calibration.

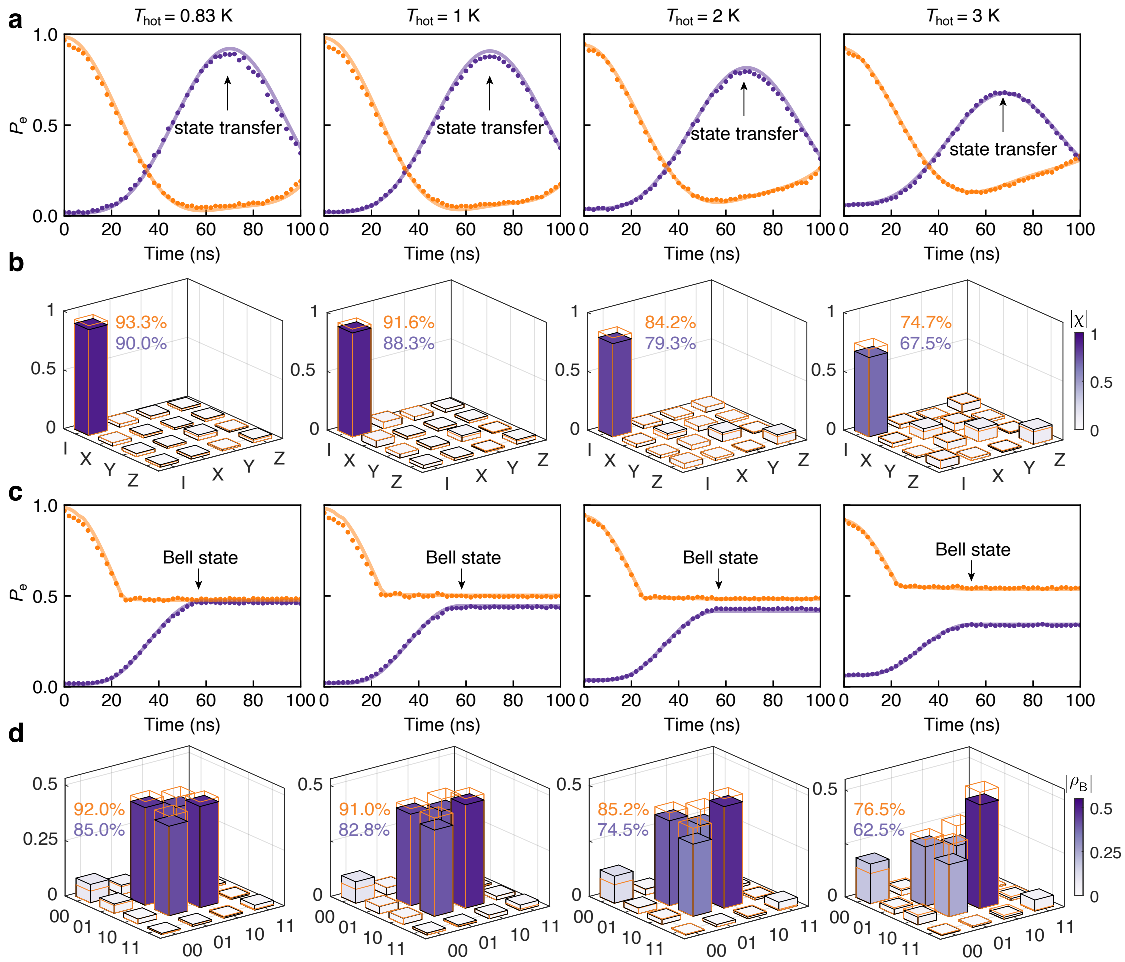

Supplementary Fig. 12. **Quantum state transfer and remote entanglement generation across various $T_{\rm hot}$.** **a**, Transferring a photon from Q_A to Q_B via R_c. Orange (purple) circles represent the excited state populations of Q_A (Q_B). The solid lines are simulations. **b**, Process matrices (χ) characterizing the quantum state transfer at $T_{\rm hot}$ = 0.83 K, 1 K, 2 K, and 3 K. Process fidelities ($\mathcal{F}_\chi$) are shown for cases without SPAM error correction (purple bars) and with SPAM error correction (orange frames). **c**, Transferring half a photon from Q_A to Q_B. **d**, Density matrices (ρ_B) for the Bell state generated at $t = 53$ ns. The corresponding fidelities ($\mathcal{F}_\rho$) are presented for cases without (purple bars) and with (orange frames) SPAM error correction.

Supplementary Fig. 12**c** presents the generation of remote entanglement between Q_A and Q_B. In this process, half a photon is first transferred from Q_A to mode R_c, which subsequently relays the state to Q_B. The Bell state fidelities, $\mathcal{F}_\rho = \langle\psi_B|\rho_B|\psi_B\rangle$, derived from raw data are 85.0%, 82.8%, 74.5%, and 62.5% for $T_{\rm hot}$ = 0.83 K, 1 K, 2 K, and 3 K, respectively. After applying SPAM correction, the fidelities improve to 92.0%, 91.0%, 85.2%, and 76.5%, as shown in Supplementary Fig. 12**d**.

The solid lines in Supplementary Figs. 12**b** and **d** represent the results of QuTiP simulations. The initial states for these simulations include thermal excitations consistent with conditions when the qubit is cooled using the D coupler. For each T_{hot}, system parameters κ_i and thermal photon numbers $\langle N_j \rangle$ $(j = A, B, c)$ and the coupling rates g_n^c $(n = A, B)$ are fitted around the values calibrated at $T_{\text{hot}} = 0.83$ K to match the experimental data. The simulated process fidelities $\mathcal{F}_\chi$ and Bell state fidelities $\mathcal{F}_\rho$ in Figs. 4**d** and **h** are obtained using the same initial states and parameters.

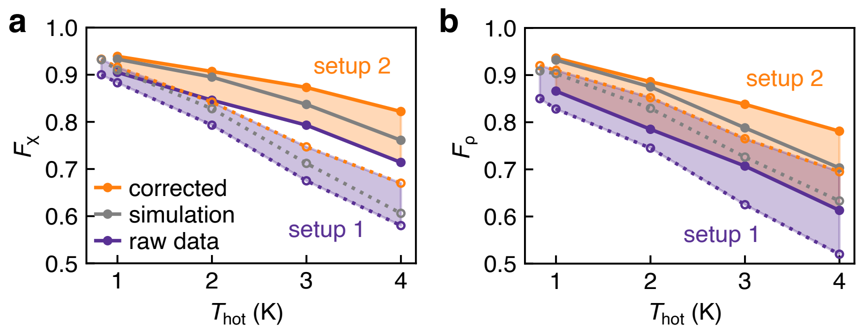

Supplementary Fig. 13. **Fidelity versus T_{hot}.** **a**, Process fidelity $\mathcal{F}\chi$ for quantum state transfer as a function of channel temperature T_{hot}. **b**, Bell state fidelity $\mathcal{F}\rho$ versus T_{hot}. open symbols and dashed lines represent data obtained from the experimental setup 1, while solid symbols and solid lines correspond to data obtained from the setup 2. The improved cable mode coherence in the setup 2 effectively mitigate thermal degradation, resulting in systematically higher fidelities across all temperatures.

To further validate the improvement brought by the setup 2, we carry out the quantum state transfer and remote entanglement generation experiment over the same temperature range. As shown in Supplementary Fig. 13, the fidelities naturally degrade with increasing T_{hot}, as expected from enhanced thermal noise and reduced qubit coherence. However, this degradation is mitigated in the setup 2 with improved cable-mode coherence. The process fidelities for quantum state transfer reach 93.9%, 90.7%, 87.3%, and 82.2% (90.5%, 84.6%, 79.3%, and 71.4% without SPAM correction) for $T_{\text{hot}} = 1$ K, 2 K, 3 K and 4 K, respectively. The corresponding Bell-state fidelities are 93.6%, 88.6%, 83.8%, and 78.1% (86.6%, 78.5%, 70.7%, and 61.3% without SPAM correction), with the extracted concurrences $C = 0.88$, 0.81, 0.72, and 0.63 ($C = 0.74$, 0.59, 0.43, and 0.25 without SPAM correction), respectively.

[1] Zhang, J. *et al.* M^2 CS: A microwave measurement and control system for large-scale superconducting quantum processors. *Chin. Phys. B* **33**, 120309 (2024).

[2] Dolan, G. J. Offset masks for lift-off photoprocessing. *Appl. Phys. Lett.* **31**, 337–339 (1977).

[3] Dunsworth, A. *et al.* Characterization and reduction of capacitive loss induced by sub-micron josephson junction fabrication in superconducting qubits. *Appl. Phys. Lett.* **111**, 22601 (2017).

[4] Chen, Z. *et al.* Fabrication and characterization of aluminum airbridges for superconducting microwave circuits. *Appl. Phys. Lett.* **104**, 52602 (2014).

[5] Dunsworth, A. *et al.* A method for building low loss multi-layer wiring for superconducting microwave devices. *Appl. Phys. Lett.* **112**, 63502 (2018).

[6] Niu, J. *et al.* Low-loss interconnects for modular superconducting quantum processors. *Nat. Electron.* **6**, 235–241 (2023).

[7] Pozar, D. M. *Microwave engineering* (Wiley, 2012), fourth edn.

[8] Chang, H.-S. *et al.* A fast and large bandwidth superconducting variable coupler. *Appl. Phys. Lett.* **117**, 244001 (2020).

[9] Satzinger, K. J. *et al.* Quantum control of surface acoustic-wave phonons. *Nature* **563**, 661–665 (2018).

[10] Bienfait, A. *et al.* Phonon-mediated quantum state transfer and remote qubit entanglement. *Science* **364**, 368–371 (2019).

[11] Zhong, Y. *et al.* Deterministic multi-qubit entanglement in a quantum network. *Nature* **590**, 571–575 (2021).

[12] Houck, A. A. *et al.* Controlling the spontaneous emission of a superconducting transmon qubit. *Phys. Rev. Lett.* **101**, 80502 (2008).

[13] Jeffrey, E. *et al.* Fast accurate state measurement with superconducting qubits. *Phys. Rev. Lett.* **112**, 190504 (2014).

[14] Walter, T. *et al.* Rapid high-fidelity single-shot dispersive readout of superconducting qubits. *Phys. Rev. Applied* **7**, 54020 (2017).

[15] Roy, T. *et al.* Broadband parametric amplification with impedance engineering: Beyond the gain-bandwidth product. *Appl. Phys. Lett.* **107**, 262601 (2015).

[16] Grebel, J. *et al.* Flux-pumped impedance-engineered broadband josephson parametric amplifier. *Appl. Phys. Lett.* **118**, 142601 (2021).

[17] Martinis, J. M., Nam, S., Aumentado, J. & Urbina, C. Rabi oscillations in a large josephson-junction qubit. *Phys. Rev. Lett.* **89**, 117901 (2002).

[18] Mallet, F. *et al.* Single-shot qubit readout in circuit quantum electrodynamics. *Nat. Phys.* **5**, 791–795 (2009).

[19] Chen, L. *et al.* Transmon qubit readout fidelity at the threshold for quantum error correction without a quantum-limited amplifier. *npj Quantum Inf.* **9**, 26 (2023).

[20] Khalil, M. S., Stoutimore, M. J. A., Wellstood, F. C. & Osborn, K. D. An analysis method for asymmetric resonator transmission applied to superconducting devices. *J. Appl. Phys.* **111**, 54510 (2012).

[21] Megrant, A. *et al.* Planar superconducting resonators with internal quality factors above one million. *Appl. Phys. Lett.* **100**, 113510 (2012).

[22] Kurpiers, P., Walter, T., Magnard, P., Salathe, Y. & Wallraff, A. Characterizing the attenuation of coaxial and rectangular microwave-frequency waveguides at cryogenic temperatures. *EPJ Quantum Technol.* **4**, 1–15 (2017).

[23] Burkhart, L. D. *et al.* Error-detected state transfer and entanglement in a superconducting quantum network. *PRX Quantum* **2**, 030321 (2021).

[24] Pekola, J. P. Towards quantum thermodynamics in electronic circuits. *Nat. Phys.* **11**, 118–123 (2015).

[25] Roßnagel, J. *et al.* A single-atom heat engine. *Science* **352**, 325–329 (2016).

[26] Ronzani, A. *et al.* Tunable photonic heat transport in a quantum heat valve. *Nat. Phys.* **14**, 991–995 (2018).

[27] Pekola, J. P. & Karimi, B. Colloquium: Quantum heat transport in condensed matter systems. *Rev. Mod. Phys.* **93**, 41001 (2021).

[28] Lu, Y. *et al.* Steady-state heat transport and work with a single artificial atom coupled to a waveguide: Emission without external driving. *PRX Quantum* **3**, 20305 (2022).

[29] Pekola, J. P. & Karimi, B. Ultrasensitive calorimetric detection of single photons from qubit decay. *Phys. Rev. X* **12**, 11026 (2022).

[30] Schuetz, M. J. A. *et al.* Quantum simulation and optimization in hot quantum networks. *Phys. Rev. B* **99**, 241302 (2019).

[31] Johansson, J., Nation, P. & Nori, F. QuTiP: An open-source python framework for the dynamics of open quantum systems. *Comput. Phys. Commun.* **183**, 1760–1772 (2012).

[32] Scigliuzzo, M. *et al.* Primary thermometry of propagating microwaves in the quantum regime. *Phys. Rev. X* **10**, 41054 (2020).

[33] Wang, Z. *et al.* Quantum microwave radiometry with a superconducting qubit. *Phys. Rev. Lett.* **126**, 180501 (2021).

[34] Lvov, D. S., Lemziakov, S. A., Ankerhold, E., Peltonen, J. T. & Pekola, J. P. Thermometry based on a superconducting qubit. *Phys. Rev. Appl.* **23**, 54079 (2025).